A Two-Time-Scale Approach for Discrete-Time Kalman Filter Design and Application to AHWR Flux Mapping

Rajasekhar Ananthoju, A. P. Tiwari, and Madhu N. Belur

***Abstract*—In large nuclear reactors such as the Advanced Heavy Water Reactor (AHWR), the core neutron flux distribution needs to be continuously monitored and displayed to the operator. This task is accomplished by an online Flux Mapping System, which employs a suitable algorithm to estimate the core flux distribution from the readings of a large number of in-core detectors. Most of the algorithms available today employ the Flux Synthesis method, Internal Boundary Condition method, and the method based on simultaneous least squares solutions of neutron diffusion and detector response equations. A common feature of these methods is the assumption that the neutron flux profile in the reactor is independent of time. Application of Kalman filtering-based approaches are also found though to a very limited extent. In this paper, we have formulated the task of flux-mapping problem in AHWR as a problem of optimally estimating the time-dependent neutron flux at a large number of mesh points in the core. The solution is obtained using the well-known Kalman filtering technique which works along with a space-time kinetics model of the reactor. However, the attempt to solve the Kalman filtering problem in a straightforward manner is not successful due to severe numerical ill-conditioning caused by the simultaneous presence of slow and fast phenomena typically present in a nuclear reactor. Hence, a grouping of state variables has been suggested whereby the original high-order model of the reactor is decoupled into a slow subsystem and a fast subsystem. Now according to the order of the slow and fast subsystems, the original time update and Kalman gain equations have also been decoupled into separate sets of equations for the slow and fast subsystems. The decoupled sets of equations could be solved easily. The proposed method has been validated in a number of typical transient situations. Overall accuracy in the estimation using the proposed methodology has been very good for mesh fluxes, channel fluxes, quadrant fluxes, and the core average flux.**

***Index Terms*—Advanced Heavy Water Reactor (AHWR), core flux distribution, discrete-time Kalman filter, flux mapping, ill-conditioning, singular perturbation, two-time-scale systems.**

Manuscript received August 17, 2015; revised November 06, 2015; accepted November 11, 2015. Date of current version February 16, 2016.

A. Rajasekhar is with the Homi Bhabha National Institute, Mumbai-400094, India (e-mail: arsbarc@gmail.com; arsekhar@barc.gov.in).

A. P. Tiwari is with the Reactor Control Systems Design Section, Bhabha Atomic Research Centre, Mumbai-400085, India and also with the Homi Bhabha National Institute, Mumbai-400094, India (e-mail: apti-wari@barc.gov.in).

M. N. Belur is with the Department of Electrical Engineering, Indian Institute of Technology Bombay, Mumbai-400076, India (e-mail: belur@ee.iitb.ac.in).

Color versions of one or more of the figures in this paper are available online at http://ieeexplore.ieee.org.

Digital Object Identifier 10.1109/TNS.2015.2500917

I. Introduction

FOR safe, reliable, and economic operation of nuclear power plants, operating power of the reactor should be maintained close to the demand power, and at the same time, the core flux distribution should closely match the desired flux distribution. Modern reactors have provisions for online spatial control and monitoring of flux or power distribution during the course of their operation. The time-varying neutron flux distribution is computed by an online Flux Mapping System (FMS), with the help of flux-mapping algorithms. The measurement signals of several in-core flux detectors are processed to generate the detailed 3-D flux map, which helps for spatial control purpose. In CANDU-6 reactors and in Indian 540 MWe Pressurized Heavy Water Reactors (PHWRs), 102 vanadium detectors are used for flux mapping, while in PWRs it is carried out by rhodium detectors installed in about 45 fuel assemblies. Over the years, research has been carried out to evolve an efficient flux-mapping algorithm for the improvement of accuracy in flux mapping with less computational effort. Most of the algorithms existing in the literature are based on three principles, namely the Flux Synthesis, Internal boundary condition, and simultaneous least squares solution of neutron diffusion and detector response equations.

The most popular and traditional method for flux mapping is known as the Flux Synthesis Method (FSM) [1]. It uses the available detector measurements and performs a least squares fit with precomputed flux modes, determined based on the reactivity devices configuration. Determination of flux modes requires the knowledge of core configuration and considerable insight into the reactor operation. There are other synthesis methods such as the Harmonic Synthesis Method (HSM) [2], [3] the and Harmonic Expansion Method (HEM) [4] to improve the accuracy of flux mapping. However, the accuracy of reconstruction depends on selection of the reference case. Selection of a suitable reference case which reflects the actual core condition results in improvement of the reconstruction accuracy. During the core configuration changes, the reference case has to be renewed, which can be a time-consuming process.

A method based on direct online solution of neutron diffusion equations with detector readings as the internal boundary condition is reported in [5], [6]. A method which obtains a least squares solution of the core neutronics design equations along with the in-core detector response equations is reported in [7]–[9]. Applicability of this least squares method requires to solve the overdetermined system of equations resulting in the framework of mapping algorithm. Another approach with the combination of FSM and least squares method, known as the modified flux synthesis method, has been proposed for the Indian 700 MWe PHWR in [10]. This method takes longer computation time than FSM does [9], and detector signal uncertainty can also deteriorate the performance of flux-mapping calculations. A common drawback of the aforesaid methods is that they fail to account for time variation of neutron flux distribution during the reactor operation and the accuracy might be degraded considerably in presence of uncertainty in the detector readings. With this motivation we have attempted discrete-time Kalman filter (DKF) formulation for flux mapping which is quite different from the existing methods, as it can take care of both time-varying phenomena and random errors in the detector readings.

The Advanced Heavy Water Reactor (AHWR) [11] is a 920 MW (thermal), vertical, pressure tube type, heavy-water moderated, boiling light-water cooled natural circulation reactor. The physical dimensions of the core are very large compared to the neutron migration length. Therefore, operational perturbations might lead to slow xenon-induced oscillations, which might cause changes in axial and radial flux distribution from the nominal distribution. Knowledge of any such changes during the reactor operation is crucial. To monitor the core flux distribution, 200 SPNDs are proposed to be provided in AHWR. An efficient flux-mapping algorithm in AHWR can ensure better reactor regulation and core monitoring, as more accurate estimates of channel and zonal powers will be available to the Reactor Regulating System (RRS) and Core Monitoring System.

In this paper, we formulate the flux-mapping problem of AHWR as a linear stochastic estimation problem and obtain the solution by the DKF technique. It utilizes the time-dependent core neutronics equations based on the nodal modeling technique [12], [13] and available detector measurements corrupted with white Gaussian noise. However, the higher order estimation model of AHWR exhibits a multi-time-scale property which results in stiffness and ill-conditioning in design. In particular, the set of recursive equations for computation of DKF gains, as a solution to weighted least squares problem, is ill-conditioned. Consequently, serious numerical difficulties are expected if the DKF gain matrix is to be computed on the basis of the full-order Riccati equation. Fortunately, this situation can easily be handled by singular perturbation analysis and two-time-scale methods. It has already been efficiently utilized in designing advanced controllers for AHWR [14]–[17]. Singular perturbation analysis and decomposition methods are reported in [18]–[22]. Singular perturbation methods in Kalman filter design are reported in [23]–[27].

We derive the estimation model for two-time-scale systems and decouple the DKF into a DKF for the slow subsystem and another for the fast subsystem using block diagonalization. Then we reformulate the problem as linear stochastic estimation problem for singularly perturbed systems. To address the numerical ill-conditioning problems in full-order design, we propose a discrete-time decoupled Kalman filtering (DDKF) technique by decoupling the DKF equations according to the order of the slow and fast subsystems. Finally this technique has been applied for estimation of detailed mesh, channel, and zonal fluxes in the AHWR.

II. Background

A. Singular Perturbation Analysis

The main purpose of the singular perturbation approach to analysis and design is to handle the ill-conditioning resulting from the interaction of slow and fast dynamic modes. Linear singularly perturbed systems can be represented [18]–[22] by the set of equations

$$\dot{x}_1 = A_{11}x_1 + A_{12}x_2 + B_1 u, \quad x_1(t_0) = x_{10} \tag{1}$$
$$\dot{x}_2 = \frac{A_{21}}{\varepsilon}x_1 + \frac{A_{22}}{\varepsilon}x_2 + \frac{B_2}{\varepsilon}u, \quad x_2(t_0) = x_{20} \tag{2}$$

and corresponding observations

$$z = \Psi_1 x_1 + \Psi_2 x_2 \tag{3}$$

where the n_1-dimensional state vector x_1 is predominantly slow and the n_2-dimensional state vector x_2 contains fast transients superimposed on a slowly varying "quasi-steady-state," i.e., $\|\dot{x}_2\| \gg \|\dot{x}_1\|$. The order of the system represented by (1) and (2) is $n = n_1 + n_2$. The scaling parameter $\varepsilon > 0$ represents the speed ratio of the slow versus fast phenomena [28]. u is the m-dimensional input vector, and z is the p-dimensional output vector. An important characteristic of the system described by (1)–(3) is that the eigenvalues are found in two widely separated clusters: n_2 eigenvalues are of large magnitude while n_1 are of small magnitude. The system described by (1)–(3) can be converted into block diagonal form as

$$\begin{bmatrix} \dot{x}_S \\ \dot{x}_F \end{bmatrix} = \begin{bmatrix} A_S & 0 \\ 0 & A_F \end{bmatrix} \begin{bmatrix} x_S \\ x_F \end{bmatrix} + \begin{bmatrix} B_S \\ B_F \end{bmatrix} u \tag{4}$$

and corresponding observations as

$$z = \begin{bmatrix} \Psi_S & \Psi_F \end{bmatrix} \begin{bmatrix} x_S \\ x_F \end{bmatrix} \tag{5}$$

such that $\sigma(A) = \sigma(A_S) \cup \sigma(A_F)$, where $\sigma(A)$ denotes the set of eigenvalues of A. The similarity transformation that is applied to the system given by (1)–(3) to obtain the system given by (4)–(5) is

$$\begin{bmatrix} x_S \\ x_F \end{bmatrix} = \begin{bmatrix} I_{n_1} - \varepsilon ML & -\varepsilon M \\ L & I_{n_2} \end{bmatrix} \begin{bmatrix} x_1 \\ x_2 \end{bmatrix} \tag{6}$$

in which I_{n_1} and I_{n_2} respectively denote n_1- and n_2-dimensional identity matrices, and L and M respectively satisfy

$$\varepsilon \dot{L} = A_{22}L - A_{21} - \varepsilon L(A_{11} - A_{12}L) \tag{7}$$
$$\varepsilon \dot{M} = -M(A_{22} + \varepsilon L A_{12}) + A_{12} + \varepsilon(A_{11} - A_{12}L)M. \tag{8}$$

L in (7) and M in (8) can be determined respectively by iterative solution of [21]

$$L_{k+1} = A_{22}^{-1}A_{21} + \varepsilon A_{22}^{-1}L_k(A_{11} - A_{12}L_k) \tag{9}$$
$$M_{k+1} = \varepsilon[(A_{11} - A_{12}L_k)M_k - M_k L_k A_{12}]A_{22}^{-1} + A_{12}A_{22}^{-1} \tag{10}$$
$$L_0 = A_{22}^{-1}A_{21}, \quad M_0 = A_{12}A_{22}^{-1}, \quad k = 0, 1, 2, \ldots. \tag{11}$$

The matrices in (4) and (5) are related to those in (1)–(3) as

$$\left.\begin{array}{c} A_S = A_{11} - A_{12}L, \quad A_F = \frac{A_{22}}{\varepsilon} + LA_{12}, \\ B_S = (I_{n_1} - \varepsilon ML)B_1 - MB_2, \\ B_F = LB_1 + \frac{B_2}{\varepsilon}, \quad \Psi_S = \Psi_1 - \Psi_2 L, \\ \text{and} \quad \Psi_F = \varepsilon\Psi_1 M + \Psi_2(I_{n_2} - \varepsilon LM) \end{array}\right\}. \tag{12}$$

The system represented by (4) and (5) can be discretized to obtain

$$\begin{bmatrix} x_{S,k} \\ x_{F,k} \end{bmatrix} = \begin{bmatrix} F_S & 0 \\ 0 & F_F \end{bmatrix} \begin{bmatrix} x_{S,k-1} \\ x_{F,k-1} \end{bmatrix} + \begin{bmatrix} G_S \\ G_F \end{bmatrix} u_{k-1} \tag{13}$$

$$z_k = [\,\Psi_S \quad \Psi_F\,] \begin{bmatrix} x_{S,k} \\ x_{F,k} \end{bmatrix} \tag{14}$$

where $F_S = e^{A_S\tau}$, $F_F = e^{A_F\tau}$, $G_S = \int_0^\tau e^{A_S\mu} B_S d\mu$, $G_F = \int_0^\tau e^{A_F\mu} B_F d\mu$, and $\tau = t_k - t_{k-1}$ is the sampling duration. For $\tau > \varepsilon$, the system represented by (13) also exhibits two-time-scale behavior, i.e., the eigenvalues of F_F will be located close to the origin of the z-plane while those of F_S will be located close to the periphery of the unit circle.

B. Discrete-Time Kalman Filter Algorithm

The DKF is an optimal recursive data processing algorithm [29], [30], also known as a linear quadratic estimator, which uses a series of measurements observed over time, containing noise (random variations) and other model inaccuracies, and produces estimates of unknown states that tend to be more precise than those based on a single measurement alone. From a Bayesian point of view, DKF propagates the conditional probability density of the desired quantities (mean and covariance), conditioned on the knowledge of the past measurements and updates it when new measurements are available. Consider a general linear discrete-time invariant stochastic system represented by

$$x_k = Fx_{k-1} + Gu_{k-1} + w_{k-1} \tag{15}$$

$$z_k = \Psi x_k + v_k. \tag{16}$$

In this, w_k and v_k are random vectors representing respectively the process and measurement noise sequences, assumed to be independent, zero mean, with white Gaussian probability distribution, and known covariances Q and R respectively, i.e.,

$$\begin{gathered} w_k \sim N(0,Q),\ E[w(t_k)] = 0,\ E[w(t_k)w^T(t_j)] = Q\delta_{kj} \\ v_k \sim N(0,R),\ E[v(t_k)] = 0,\ E[v(t_k)v^T(t_j)] = R\delta_{kj} \\ E[v(t_k)w^T(t_j)] = 0 \end{gathered}$$

where Q is positive-semidefinite matrix and R is positive-definite matrix. $E[\cdot]$ is expectation operator and δ_{kj} is the Kronecker delta function, i.e., $\delta_{kj} = 1$ if $k = j$, and $\delta_{kj} = 0$ if $k \neq j$. The initial state x_0 is also a Gaussian random variable, independent of the noise processes, with $x_0 \sim N(\hat{x}_0, P_0)$. Therefore $E[x_0] = \hat{x}_0, E[(x - \hat{x}_0)(x - \hat{x}_0)^T] = P_0$, where $\hat{x}$ is state estimate, P is the covariance of the error in the estimated state. The DKF equations for the above system fall into two groups, namely time update equations and the measurement update equations.

1) Time Update Equations: These equations, also known as state and covariance prediction equations, project forward (in time) the current state and error covariance estimates to obtain *a priori* estimates for the next step, i.e.,

$$\hat{x}_k^- = F\hat{x}_{k-1} + Gu_{k-1} \tag{17}$$

$$P_k^- = FP_{k-1}F^T + Q. \tag{18}$$

2) Measurement Update Equations: These equations incorporate a new measurement z_k into an *a priori* estimate to obtain an improved *a posteriori* estimate, i.e.,

$$K_k = P_k^- \Psi^T [\Psi P_k^- \Psi^T + R]^{-1} \tag{19}$$

$$\hat{x}_k = \hat{x}_k^- + K_k[z_k - \Psi\hat{x}_k^-] \tag{20}$$

$$P_k = [I - K_k\Psi]P_k^-. \tag{21}$$

III. Two-Time-Scale Approach for Discrete-Time Kalman Filter design

Direct implementation of the DKF algorithm to a high-order stiff system, such as the nuclear reactor is not feasible due to numerical ill-conditioning. However, utilizing the block diagonalized model (13) and (14), the time and measurement update equations discussed in Section II-B can be decoupled according to the order n_1 of the slow and order n_2 of the fast subsystems. A high-order stochastic system such as the one represented by (15) and (16) possessing two-time-scale behavior can be represented into linear singularly perturbed form and block-diagonalized as described in Section II-A, to obtain

$$\begin{bmatrix} x_{S,k} \\ x_{F,k} \end{bmatrix} = \begin{bmatrix} F_S & 0 \\ 0 & F_F \end{bmatrix} \begin{bmatrix} x_{S,k-1} \\ x_{F,k-1} \end{bmatrix} + \begin{bmatrix} G_S \\ G_F \end{bmatrix} u_{k-1} + \begin{bmatrix} w'_{S,k-1} \\ w'_{F,k-1} \end{bmatrix} \tag{22}$$

$$z_k = [\,\Psi_S \quad \Psi_F\,] \begin{bmatrix} x_S \\ x_F \end{bmatrix} + \begin{bmatrix} v_{S,k-1} \\ v_{F,k-1} \end{bmatrix} \tag{23}$$

where the additional terms w'_S, v_S, and v_F follow from (15) and (16). The matrices P and Q appearing in (18) can also be partitioned according to the orders of the slow and fast subsystems and from (18), we have

$$\begin{aligned} P_k^- &= \begin{bmatrix} P_{11,k}^- & P_{12,k}^- \\ P_{12,k}^{-\,T} & P_{22,k}^- \end{bmatrix} \\ &= \begin{bmatrix} F_S & 0 \\ 0 & F_F \end{bmatrix} \begin{bmatrix} P_{11,k-1} & P_{12,k-1} \\ P_{12,k-1}{}^T & P_{22,k-1} \end{bmatrix} \begin{bmatrix} F_S{}^T & 0 \\ 0 & F_F{}^T \end{bmatrix} \\ &\quad + \begin{bmatrix} Q_{11} & Q_{12} \\ Q_{12}{}^T & Q_{22} \end{bmatrix}. \end{aligned} \tag{24}$$

Thus, we have

$$P_{11,k}^- = F_S P_{11,k} F_S^T + Q_{11} \tag{25}$$

$$P_{22,k}^- = F_F P_{22,k} F_F^T + Q_{22} \tag{26}$$

$$P_{12,k}^- = F_S P_{12,k} F_F^T + Q_{12}. \tag{27}$$

Similarly, (19) can be written as

$$\begin{aligned} K_k = \begin{bmatrix} K_{S,k} \\ K_{F,k} \end{bmatrix} &= \begin{bmatrix} P_{11,k}^- & P_{12,k}^- \\ P_{12,k}^{-\,T} & P_{22,k}^- \end{bmatrix} \begin{bmatrix} \Psi_S^T \\ \Psi_F^T \end{bmatrix} \\ &\times \left\{ \begin{bmatrix} \Psi_S^T \\ \Psi_F^T \end{bmatrix}^T \begin{bmatrix} P_{11,k}^- & P_{12,k}^- \\ P_{12,k}^{-\,T} & P_{22,k}^- \end{bmatrix} \begin{bmatrix} \Psi_S^T \\ \Psi_F^T \end{bmatrix} + R \right\}^{-1}. \end{aligned} \tag{28}$$

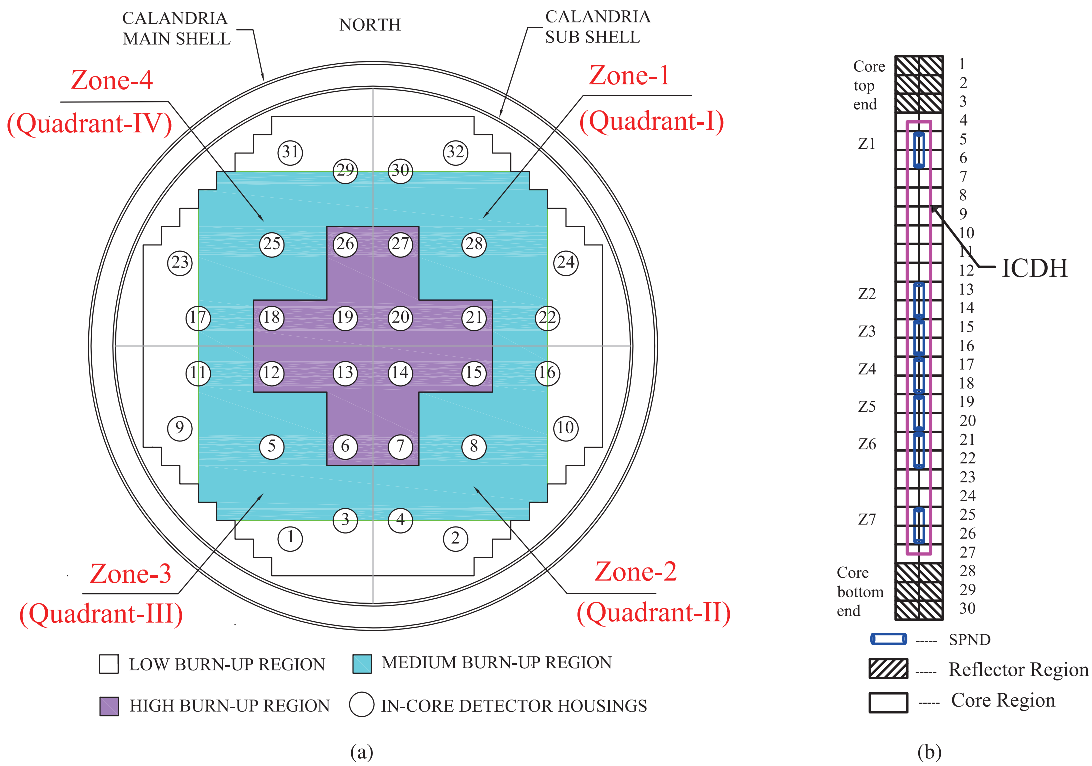

Fig. 1. AHWR core layout (schematic). (a) AHWR Core layout with ICDH Locations. (b) Placement of SPNDs in ICDH.

Hence

$$K_{S,k} = (P^-_{11,k}\Psi_S^T + P^-_{12,k}\Psi_F^T)Y^{-1} \tag{29}$$
$$K_{F,k} = (P^{-T}_{12,k}\Psi_S^T + P^-_{22,k}\Psi_F^T)Y^{-1} \tag{30}$$

where

$$Y = \Psi_S P^-_{11,k}\Psi_S^T + 2\Psi_S P^-_{12,k}\Psi_F^T + \Psi_F P^-_{22,k}\Psi_F^T + R \tag{31}$$

and

$$\begin{aligned} P_k &= \begin{bmatrix} P_{11,k} & P_{12,k} \\ P_{12,k}{}^T & P_{22,k} \end{bmatrix} \\ &= \left\{ \begin{bmatrix} I_{n1} & 0 \\ 0 & I_{n2} \end{bmatrix} - \begin{bmatrix} K_{S,k} \\ K_{F,k} \end{bmatrix} \begin{bmatrix} \Psi_S^T \\ \Psi_F^T \end{bmatrix}^T \right\} \begin{bmatrix} P^-_{11,k} & P^-_{12,k} \\ P^{-T}_{12,k} & P^-_{22,k} \end{bmatrix} \end{aligned} \tag{32}$$

which yields

$$P_{11,k} = (I_{n1} - K_{S,k}\Psi_S)P^-_{11,k} - K_{S,k}\Psi_F P^{-T}_{12,k} \tag{33}$$
$$P_{22,k} = (I_{n2} - K_{F,k}\Psi_F)P^-_{22,k} - K_{F,k}\Psi_S P^-_{12,k} \tag{34}$$
$$P_{12,k} = (I_{n1,n2} - K_{S,k}\Psi_S)P^-_{12,k} - K_{S,k}\Psi_F P^-_{22,k}. \tag{35}$$

Note that the covariance equation of time update step is decoupled into three equations given by (25)–(27); the measurement update step is decoupled into three equations given by (33)–(35), and the Kalman gain equation is decoupled into two equations given by (29)–(30). Hence the proposed DKF algorithm for the singularly perturbed system has total ten equations.

IV. Development of Flux Estimation Model for AHWR

The DKF-based flux-mapping technique is applied to AHWR, a Th-Pu-based boiling water cooled, heavy-water moderated thermal reactor. Its core consists of 513 lattice positions, 452 of which are occupied by fuel assemblies and the remaining by control and shut-off rods. Fig. 1(a) shows the layout of AHWR core. In-core Detector Housings (ICDHs) located at 32 interlattice locations, accommodate the Self-Powered Neutron Detectors (SPNDs) which are used for thermal neutron flux measurement. These SPNDs are provided at different elevations of the assembly covering the entire AHWR core from top to bottom. Fig. 1(b) shows the housing of seven detectors in one of those intralattice locations, in which $z_1, z_2, \ldots, z_7$ indicate the locations where SPNDs have been proposed to be placed.

A. Mathematical Modeling of AHWR

For the purpose of estimation of neutron flux in the AHWR core, using the DKF-based algorithm, a reasonably accurate space-time kinetics model is required. In [12], a 17-node scheme, which exhibits all the essential control-related properties and yields accurate transient response characteristics, is derived. The same model is reformulated in terms of neutron flux equations in [13]. This model is more suitable for flux distribution studies owing to its simplicity and the structure, thus facilitating selection of state variables for the system in a straightforward manner. It assumes that the reactor spatial domain is divided into relatively large number of rectangular parallelopiped shaped regions called nodes which are coupled through neutron diffusion. Neutron flux and other parameters in each node are represented by homogenized values integrated over its volume, and the degree of coupling among these nodes

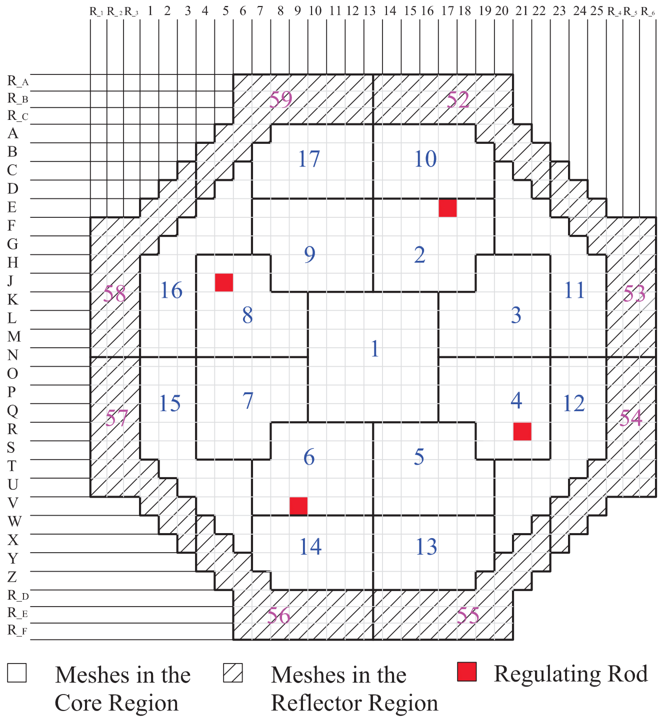

Fig. 2. Seventeen-node scheme.

is given by coupling coefficients. The following set of nonlinear time-dependent core neutronics equations and the associated equations for the delayed neutron precursors represents the nodal core model of AHWR:

$$\frac{d\phi_h}{dt} = -\omega_{hh}\upsilon_h\phi_h + \sum_{k=1}^{N_h}\omega_{hk}\upsilon_h\phi_k + (\rho_h - \beta)\frac{\phi_h}{\ell_h} + \sum_{i=1}^{m}\upsilon_h\lambda_i C_{ih}, \quad h = 1,2,\ldots,Z_p \tag{36}$$

$$\frac{dC_{ih}}{dt} = \frac{\beta_i\phi_h}{\upsilon_h\ell_h} - \lambda_i C_{ih}, \quad i = 1,2,\ldots,m \tag{37}$$

where ϕ_h denotes neutron flux in node h; C_{ih} denotes delayed neutron precursor concentration for group i in node h; β_i and λ_i denote neutron fraction yield and decay constant for group i respectively; υ_h denotes mean velocity of neutron in node h; and ℓ_h denotes prompt neutron life time. The coupling coefficients ω_{hk} depend on the geometry, material composition, and characteristic distance between the nodes h and k. Fission reactions do not take place in reflector region. However, the neutron leakage to reflector needs to be taken into account. Thus, for the nodes in the reflector region, the flux variation taking place can be described as

$$\frac{d\phi_h}{dt} = -\omega_{hh}\upsilon_h\phi_h + \sum_{k=1}^{N_h}\omega_{hk}\upsilon_h\phi_k, \quad h = Z_p+1,\ldots,Z_p+Z_r. \tag{38}$$

The AHWR core is considered to be divided into 17 nodes as shown in Fig. 2. There are eight regulating rods (RRs) from which four are in manual mode. The other four RRs located in nodes 2, 4, 6, and 8 are under automatic control. The top and bottom reflector regions are divided into 17 nodes each, in identical manner as the core, whereas the side reflector is divided into eight nodes, giving 59 nodes in all. Thus, in (36) and (38), $Z_p = 17$ and $Z_r = 42$. For further simplicity, only one effective group of delayed neutrons is considered, i.e., in (37), $m = 1$ and internal reactivity feedbacks are not considered. Besides, in small-scale transients involving normal operational and control situations, in which the flux-mapping task is of significance, reactivity control requirements are fulfilled only by regulating rods, i.e., ρ_h is essentially on account of RR movements. Reactivity contributed by the movement of a RR is a nonlinear function of its position. However, around the equilibrium position, the nonlinearity is very insignificant. Thus, the reactivity in node h due to the movement of RR in it is given by

$$\rho_h = (-10.234H_l + 676.203) \times 10^{-6}. \tag{39}$$

Each RR is attached through a rope-pulley mechanism to the respective reversible variable speed type RR drive having individual three phase induction motors and static frequency converters. Neglecting the friction, damping, and rotational to linear motion transmission dynamics, the speed of the regulating rod is directly proportional to the applied voltage ϑ_l to the drive motor, i.e.,

$$\frac{dH_l}{dt} = K_{RR}\vartheta_l, \qquad l = 1,\ldots,8 \tag{40}$$

where $K_{RR} = 0.56$.

In [13], a scheme for obtaining detailed core flux distribution from the 17 nodal fluxes and 42 reflector fluxes computed by solving (36)–(38) is given. According to this scheme, the values of neutron fluxes in 22 950 small volume elements are determined as

$$\phi_V = W_V\phi_C \tag{41}$$

where ϕ_V denotes a vector of 22 950 flux values, ϕ_C denotes the vector of flux values obtained from (36)–(38) and W_V is a weighting matrix determined based on detailed 3-D flux distribution computations. Subsequently the fluxes at SPND locations are obtained from

$$\phi_D = W_D\phi_V \tag{42}$$

where ϕ_D denotes the vector of fluxes at SPND locations and W_D is a weighting matrix. Combining (41) and (42), we have

$$\phi_D = W_D W_V\phi_C = W_{DV}\phi_C. \tag{43}$$

Thus, the fluxes at SPNDs locations are obtained from nodal fluxes. The SPNDs are assumed to give output signal proportional to local fluxes, i.e., dynamic effects are ignored.

B. Derivation of Estimation Model

To obtain the estimation model, the system of nonlinear equations (36)–(40) is linearized around the steady-state operating point (ϕ_{h0}, C_{h0}), by considering a small perturbation in neutron flux level, delayed neutron precursor concentration, RR position, and the input voltages to RR drives, denoted respectively by $\delta\phi_h, \delta C_h, \delta H_h$, and $\delta\vartheta_h$ around the operating point. Then from (36), (37), (38), and (40), we have

$$\frac{d\delta\phi_h}{dt} = \left[-\omega_{hh}v_h + \frac{\rho_{i0}}{\ell_i} - \frac{\beta}{\ell_h}\right]\delta\phi_h + \sum_{k=1}^{N_h}\omega_{hk}v_h\left(\frac{\phi_{k0}}{\phi_{h0}}\right)\delta\phi_k + \frac{\beta}{\ell_h}\delta C_h - \frac{10.234\times10^{-6}\times\phi_{h0}}{\ell_h}\delta H_h,\quad h=1,2,3,\ldots,Z_p \tag{44}$$

$$\frac{d\delta C_h}{dt} = \lambda\delta\phi_h - \lambda\delta C_h \tag{45}$$

$$\frac{d\delta\phi_h}{dt} = -\omega_{hh}v_h\delta\phi_h + \sum_{k=1}^{N_h}\omega_{hk}v_h\left(\frac{\phi_{k0}}{\phi_{h0}}\right)\delta\phi_k \tag{46}$$

$$h = Z_p+1,..,Z_p+Z_r,$$

$$\frac{d\delta H_l}{dt} = K_{RR}\delta\vartheta_l,\quad l=2,4,6,8 \tag{47}$$

where δ denotes the deviation from respective steady-state values. In (44), the term δH_l denoting the deviation in position of the lth RR from that corresponding to the critical configuration will be present only if the node h contains the RR-l. Now, define the state vector as

$$x = [\,x_{\phi_C}^T \quad x_C^T \quad x_{\phi_R}^T \quad x_H^T\,]^T \tag{48}$$

where

$$x_{\phi_C} = [\,\delta\phi_1/\phi_{1_0} \quad \ldots \quad \delta\phi_{17}/\phi_{17_0}\,]^T \tag{49}$$

$$x_C = [\,\delta C_1/C_{1_0} \quad \ldots \quad \delta C_{17}/\phi_{17_0}\,]^T \tag{50}$$

$$x_{\phi_R} = [\,\delta\phi_{18}/\phi_{18_0} \quad \ldots \quad \delta\phi_{59}/\phi_{59_0}\,]^T \tag{51}$$

$$x_H = [\,\delta H_2 \quad \delta H_4 \quad \delta H_6 \quad \delta H_8\,]^T. \tag{52}$$

Also, define the input vector as

$$u = [\,\delta\vartheta_2 \quad \delta\vartheta_4 \quad \delta\vartheta_6 \quad \delta\vartheta_8\,]^T. \tag{53}$$

Then, (44)–(47) which constitute the estimation model can be represented in standard linear state space form of (1)–(3). The system matrix A of size 80×80 is expressed as

$$A = \begin{bmatrix} A_{\phi_C\phi_C} & A_{\phi_C C} & A_{\phi_C\phi_R} & A_{\phi_C H} \\ A_{C\phi_C} & A_{CC} & 0 & 0 \\ A_{\phi_R\phi_C} & 0 & A_{\phi_R\phi_R} & 0 \\ 0 & 0 & 0 & 0 \end{bmatrix}. \tag{54}$$

The input matrix is given as

$$B = [\,0 \quad 0 \quad 0 \quad B_H^T\,]^T \tag{55}$$

and the output matrix is given as

$$\Psi = [\,W_{DV} \quad 0 \quad 0 \quad 0\,] \tag{56}$$

where

$$A_{\phi_C\phi_C}(i,j) = \begin{cases} -\omega_{ij}v_i + \frac{\rho_{i0}}{\ell_i} - \frac{\beta}{\ell_i} & \text{if } (i=j) \\ \omega_{ij}v_i\frac{\phi_{j0}}{\phi_{i0}} & \text{if } (i\neq j) \end{cases}$$

$$A_{\phi_C C} = -\beta\times diag.\left[\,\tfrac{1}{\ell_1} \quad \tfrac{1}{\ell_2} \quad \cdots \quad \tfrac{1}{\ell_{Z_P}}\,\right]$$

$$A_{\phi_C\phi_R}(i,j) = \begin{cases} -\omega_{ij}v_i & \text{if } (i=j) \\ \omega_{ij}v_i\frac{\phi_{j0}}{\phi_{i0}} & \text{if } (i\neq j) \end{cases}$$

$$A_{\phi_C H}(i,j) = \begin{cases} -10.234\times10^{-6}\times\frac{\phi_{i0}}{\ell_h} & \text{for } (i=2,4,6,8),\ j=i/2 \\ 0 & \text{otherwise.} \end{cases}$$

$$A_{C\phi_C} = diag.[\,\lambda_1 \quad \lambda_2 \quad \ldots \quad \lambda_c\,]$$

$$A_{CC} = -diag.[\,\lambda_1 \quad \lambda_2 \quad \ldots \quad \lambda_c\,]$$

$$A_{\phi_R\phi_R}(i,j) = \begin{cases} -\omega_{ij}v_i & \text{if } (i=j) \\ \omega_{ij}v_i\frac{\phi_{j0}}{\phi_{i0}} & \text{if } (i\neq j) \end{cases}$$

$$A_{\phi_R\phi_C} = A_{\phi_C\phi_R}^T$$

$$B_H = diag.[\,K_{RR} \quad K_{RR} \quad K_{RR} \quad K_{RR}\,].$$

The eigenvalues of the system matrix A of AHWR are reported in [31], from which it can be noticed that they fall into two distinct clusters: one of 21 eigenvalues located very close to the origin of the complex s-plane and the other of 59 eigenvalues located between -475.15 and -8.4578. This suggests the presence of two-time-scale property in the estimation model. Therefore, state variables are regrouped as

$$x_1 = [\,x_H^T \quad x_C^T\,]^T \tag{57}$$

$$x_2 = [\,x_{\phi_R}^T \quad x_{\phi_C}^T\,]^T. \tag{58}$$

Now, the system, input, and output matrices given by (54)–(56) are partitioned into block matrices according to the new state vectors defined. Thus in (1)–(3) we have

$$A_{11} = \begin{bmatrix} 0 & 0 \\ 0 & A_{CC} \end{bmatrix} \qquad A_{12} = \begin{bmatrix} 0 & 0 \\ 0 & A_{C\phi_C} \end{bmatrix}$$

$$A_{21} = \begin{bmatrix} 0 & 0 \\ A_{\phi_C H} & A_{\phi_C C} \end{bmatrix} \qquad A_{22} = \begin{bmatrix} A_{\phi_R\phi_R} & A_{\phi_R\phi_C} \\ A_{\phi_C\phi_R} & A_{\phi_C\phi_C} \end{bmatrix};$$

$$B_1 = [\,B_H^T \quad 0\,]^T \qquad B_2 = [\,0 \quad 0\,]^T$$

$$\Psi_1 = [\,0 \quad 0\,] \qquad \Psi_2 = [\,0 \quad W_{DV}\,].$$

Now, the full-order system is block diagonalized using the similarity transformation (6), in which the L and M matrices for the transformation are obtained by the iterative solution of (9) and (10) respectively. Thereafter $A_S, A_F, B_S, B_F, \Psi_S$, and Ψ_F of the decoupled system represented by (4)–(5) are obtained by (12). It is observed that 59 magnitudewise largest eigenvalues of A are equal to eigenvalues of A_F, and the remaining 21 eigenvalues are equal to eigenvalues of A_S. This confirms that the estimation model is decoupled into slow and fast subsystems of order 21 and 59 respectively.

V. Application to AHWR Flux Mapping

Now the method presented in Section III has been applied for flux mapping in the core of AHWR, which is presented in Section IV. The estimation model represented by (4)–(5) is discretized for sampling time $\tau = 0.2$ s for which the discrete-time system is observed to possess the two-time-scale property.

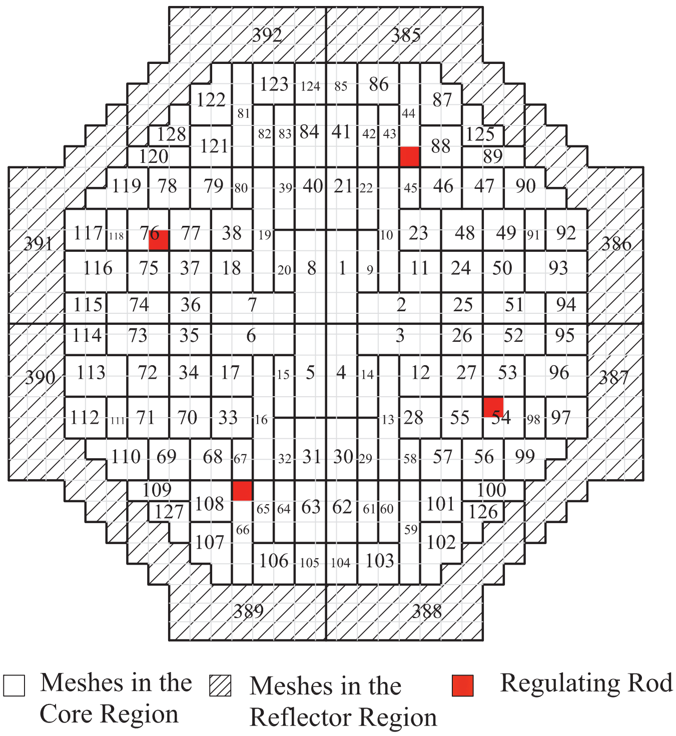

Fig. 3. One hundred twenty-eight-node scheme.

The effectiveness of the Kalman filtering technique for flux mapping has been examined in three cases. In the first case, decay of the nonzero initial condition is observed. The states of the estimation model are nonzero, while the reactor is assumed to be at steady-state. In the second, the movement of one or multiple RRs is simulated. Finally in the third case, xenon-induced spatial oscillation is considered. These cases are elaborated in the following subsections.

SPND signals (measurements) were generated under the same transient situations from a separate set of offline computations using a 128-node scheme as shown in Fig. 3, for the first two cases, and the 17-node scheme as shown in Fig. 2 for the third case. In the 128-node scheme, the core region, top reflector region, and bottom reflector region each are divided into 128 nodes, and the side reflector region is divided into eight nodes, giving 392 nodes in all. From the operational 540 MWe PHWR units 3 and 4 of the Tarapur Atomic Power Station (TAPS), India, it was revealed that noise in the signals of detectors takes normal probability distribution with a standard deviation of nearly 2% [32]. Hence, measurement noise of the order of 2% has been assumed for each SPND. This noise is equivalent to 2% random fluctuations around the full-power steady-state value in each detector.

Using the methodology suggested in [13], reference flux values have been generated for 22 950 volume elements, 452 fuel channels, four quadrants, and the core average flux denoted respectively as ϕ_v, ϕ_z, ϕ_q, and ϕ_G. The state estimation is carried out using the DKF algorithm with

$$Q = 0.1 \times I_{80} \quad \text{and} \quad R = I_{200}$$

where I_{80} and I_{200} denote identity matrices of size 80 and 200 respectively. Estimates for fluxes in 22 950 volume elements are obtained as

$$\hat{\phi}_v = W_{MX}\hat{x}_{\phi C} \tag{59}$$

where W_{MX} denotes the weighting matrix for flux reconstruction. Now, from the estimates of flux in 22 950 volume elements, the average values of channel fluxes are obtained as

$$\hat{\phi}_z = \sum_{i\in z} \hat{\phi}_{v_i} V_i \Big/ \sum_{i\in z} V_i \tag{60}$$

where V_i denotes the volume of the ith mesh box, z denotes fuel channels in core, as shown in Fig. 2. Similarly, the estimated values of quadrant fluxes are computed from

$$\hat{\phi}_q = \sum_{i\in q} \hat{\phi}_{v_i} V_i \Big/ \sum_{i\in q} V_i \tag{61}$$

where $q =$ I, II, III, and IV. Estimated value of core average flux is computed as

$$\hat{\phi}_G = \sum_{i=1}^{10848} \hat{\phi}_{v_i} V_i \Big/ \sum_{i=1}^{10848} V_i. \tag{62}$$

The values of these quantities, as determined using the DKF algorithm, are compared with their respective reference values for assessment of reconstruction accuracy. To characterize the performance of the DKF, we compute relative errors in estimation of flux in 22 950 volume elements, 452 coolant channels, and four quadrants, and also the error in the estimation of the core average flux, respectively using

$$e_{v_{i_{rel}}} = \frac{\hat{\phi}_{v_i} - \phi_{v_i}}{\phi_{v_i}} \times 100, \quad i = 1, 2, \ldots, 22950 \tag{63}$$

$$e_{z_{i_{rel}}} = \frac{\hat{\phi}_{z_i} - \phi_{z_i}}{\phi_{z_i}} \times 100, \quad i = 1, 2, \ldots, 452 \tag{64}$$

$$e_{q_{i_{rel}}} = \frac{\hat{\phi}_{q_i} - \phi_{q_i}}{\phi_{q_i}} \times 100, \quad i = I, II, III, IV \tag{65}$$

$$e_{G_{rel}} = \frac{\hat{\phi}_G - \phi_G}{\phi_G} \times 100. \tag{66}$$

RMS percentage error in flux is also calculated for volume elements and channels using

$$e_{v_{rms}} = \sqrt{\frac{1}{22950}\sum_{i=1}^{22950}\left(\hat{\phi}_{v_i} - \phi_{v_i}\right)^2} \times 100 \tag{67}$$

$$e_{z_{rms}} = \sqrt{\frac{1}{452}\sum_{i=1}^{452}\left(\hat{\phi}_{z_i} - \phi_{z_i}\right)^2} \times 100. \tag{68}$$

A. Response of DKF to Nonzero Initial Condition of Estimation Model

The reactor is assumed to be under steady-state full-power operation such that the delayed neutron precursor concentrations in different nodes are in equilibrium with the respective

TABLE I
TEST CASES AND DESCRIPTION

S. No.	Test case	Description
1	1 RR	Movement of RR in Q-I, other 3 RRs are stationary
2	2 RR	Simultaneous movement of RRs in Q-I and Q-III, other 2 RRs are stationary
3	4 RR	Simultaneous movement of RRs in Q-I, Q-II, Q-III and Q-IV
4	2 RR-D	Simultaneous movement of RRs in Q-I and Q-III in opposite directions, other 2 RRs are stationary

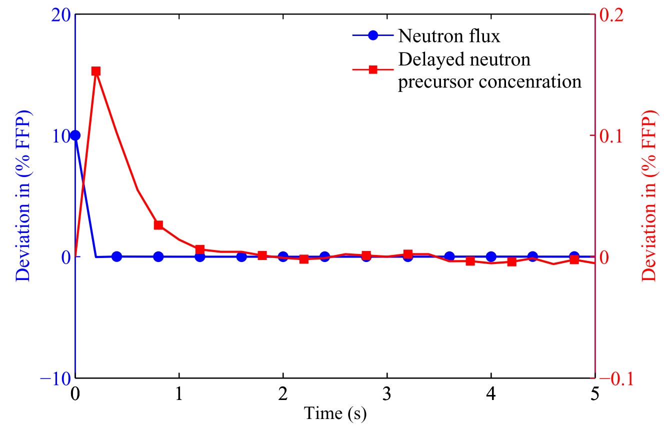

Fig. 4. Variation in the estimated values of neutron flux and delayed neutron precursor concentration in node 1.

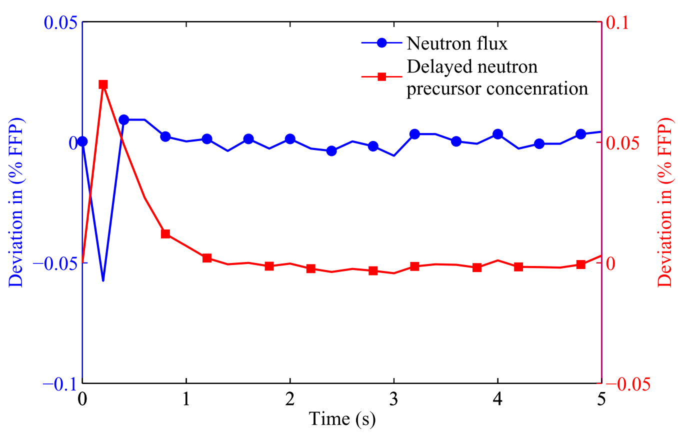

Fig. 5. Variation in the estimated values of neutron flux and delayed neutron precursor concentration in node 2.

nodal flux levels and RRs are at 66.7% in position, which corresponds to critical core configuration. As already stated, SPND signals were generated from offline computations using the 128-node scheme. At steady-state, their signals are constant but measurement noise of 2% has been introduced for each detector.

The initial estimate for neutron flux in node 1 of the AHWR core is assumed to be deviating from the actual value by 10%, while the state estimates for neutron flux in the remaining nodes x_C, x_{ϕ_R}, and x_H are assumed to be identical to their actual values. Now, the DKF algorithm is processed using the values of Q and R as mentioned earlier. The values of estimated neutron flux and delayed neutron precursor concentrations in node 1, 2, and 15 of AHWR are shown in Figs. 4, 5, and 6, respectively. The estimated states gradually approach zero in short duration of time. Such a response is considered to be satisfactory.

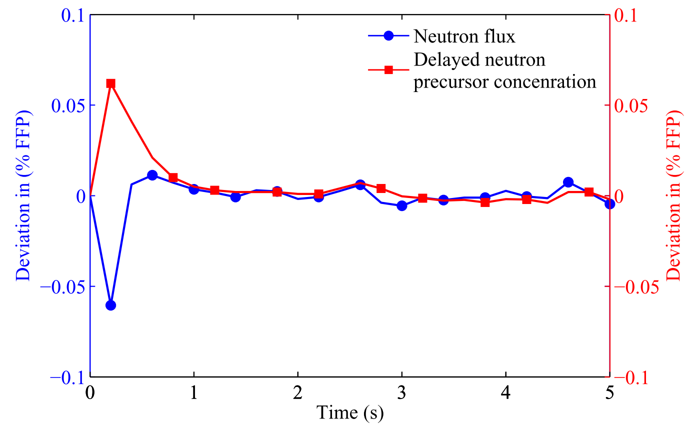

Fig. 6. Variation in the estimated values of neutron flux and delayed neutron precursor concentration in node 15.

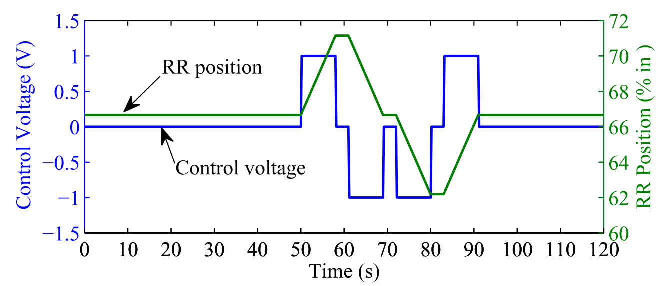

Fig. 7. Position of RR corresponding to applied control signal.

B. Movement of Regulating Rods

This simulation involves movement of one or multiple RRs as listed in Table I. At steady-state full-power operation, RRs are at 66.7% in position. In each case, the reactor is at steady-state for the initial 50 s. At time $t = 50$ s, control signal of 1 V is applied to RR drive and maintained for 8 s. Corresponding RRs move linearly into the reactor core, as governed by (40) and reach 71.14% in position. Then, the control signal is made 0 V to hold the RRs at the new position. After 3 s, the RR is driven out linearly to nominal position by applying a control signal of -1 V. Again after 3 s, an outward movement followed by inward movement back to its nominal position is simulated.

First, movement of RR located in Quadrant-I is considered. Fig. 7 shows the applied control voltage to RR drive and corresponding position of the RR in the core during the test case. Fig. 8 shows the core average flux and the relative error in the estimation of the core average flux. Fig. 9 shows the average values of flux in Quadrants-I and II of the reactor. Axial flux distribution for 24 volume elements in the channel E16X, which is near to RR, is shown in Fig. 10. Flux distribution in channel

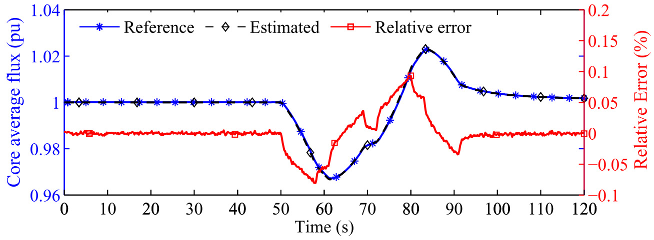

Fig. 8. Core average flux along with relative error (%) during the transient involving the movement of RR in Quadrant-I.

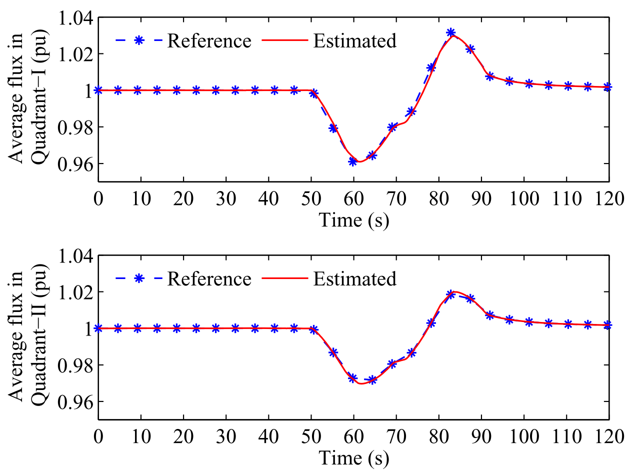

Fig. 9. Average flux in Quadrants I and II during the transient involving the movement of RR in Quadrant-I.

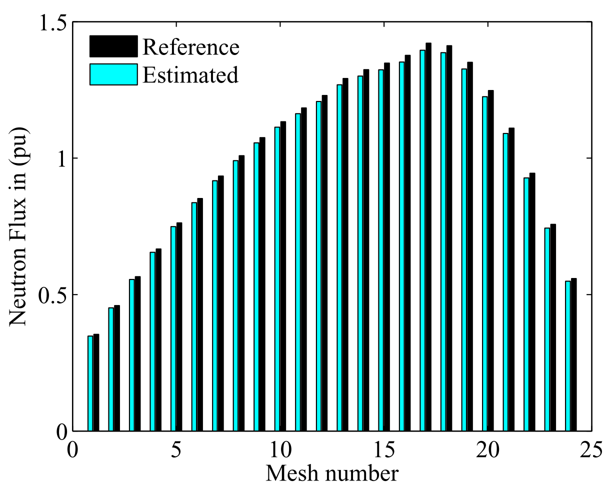

Fig. 10. Axial flux distribution in the channel E16 (in the vicinity of RR), where maximum errors occur.

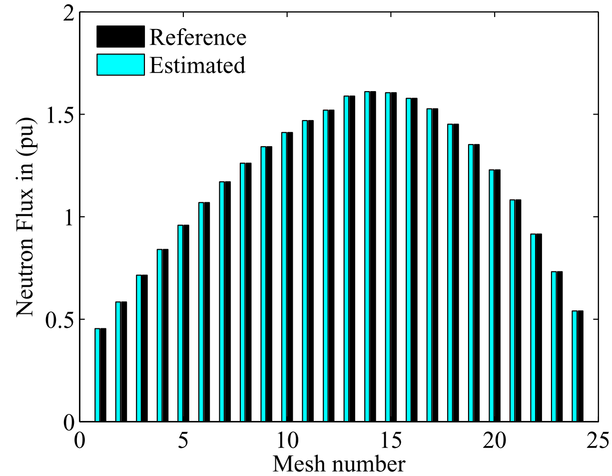

Fig. 11. Axial flux distribution in the channel N20 (away from RR), where minimum errors occur.

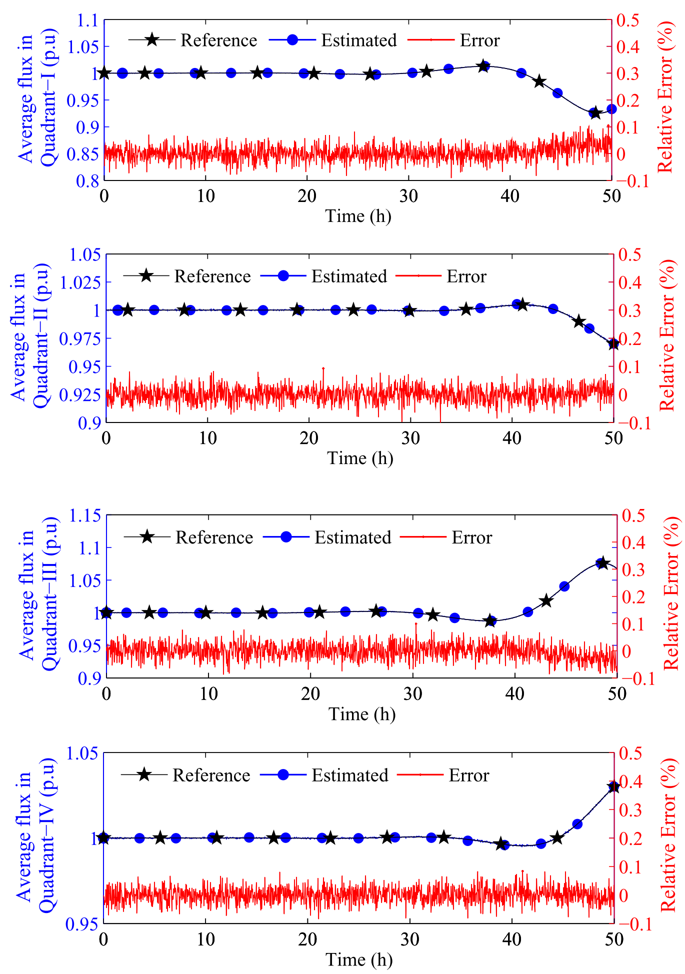

Fig. 12. Average flux in Quadrants I, II, III, and IV during the transient involving xenon oscillations.

N20, where minimum error occurs is shown in Fig. 11. Maximum RMS error in the estimation of flux occurs at $t = 80$ s for the applied transient as shown in Table II.

To asses the performance of DKF algorithm further, similar analysis is carried out for the remaining test cases listed in Table I. RMS error between estimated and reference distribution were computed and are shown in Table III. At the instant when the maximum RMS error occurred, absolute relative average errors (%) in fluxes are computed and shown in Table IV. Channelwise maximum and minimum relative errors (%) are shown in Table V. Absolute relative error in quadrant fluxes and core average fluxes are also computed and shown in Table VI.

It is worthy to note from the numerical values presented in Table III–VI that the average relative error and maximum RMS error in quadrant fluxes are 0.31% and 0.34% respectively; in case of channel fluxes they are 0.37% and 0.57% respectively;

TABLE II
MAXIMUM RMS ERROR IN ESTIMATION OF FLUX IN THE TRANSIENT INVOLVING MOVEMENT RR

S.No	Parameter	Error (%)
1	RMS error in estimation of fluxes in 22950 mesh boxes, $e_{z_{rms}}$	0.3040
2	RMS error in estimation of fluxes in 452 fuel channels, $e_{v_{rms}}$	0.3381
3	RMS error in estimation of fluxes in 4 quadrants	0.1592

TABLE III
MAXIMUM RMS ERROR (%) IN FLUXES

Test Case	Quadrants (4)	Channels		All Mesh boxes (22950)
		Fuel locations (452)	All locations (513)	
1 RR*	0.1939	0.3381	0.3457	0.3040
2 RR*	0.2431	0.4320	0.4404	0.3946
4 RR*	0.3406	0.5647	0.5766	0.5112
2 RR-D#	0.2861	0.5014	0.5139	0.4410

* Max. RMS Error Occurred at $t = 80$ s.
# Max. RMS Error Occurred at $t = 58$ s.

TABLE IV
ABSOLUTE RELATIVE AVERAGE ERROR (%) IN FLUXES

Test case	Quadrants (4)	Channels		Mesh boxes		
		Fuel locations (452)	All locations (513)	Core (10848)	Reflector (12102)	Total (22950)
1 RR	0.1196	0.1899	0.1895	0.1895	0.2396	0.2127
2 RR	0.1813	0.2557	0.2551	0.2551	0.3995	0.3220
4 RR	0.3171	0.3589	0.3617	0.3617	0.6883	0.5108
2 RR-D	0.2316	0.3705	0.3695	0.3695	0.4515	0.4075

TABLE V
MAXIMUM AND MINIMUM RELATIVE ERROR (%) IN CHANNELS

Test case	Negative				Positive			
	Maximun	Location	Minimum	Location	Maximun	Location	Minimum	Location
1 RR	1.7987	E16	0.0036	S24	0.4700	J14	0.0002	N20
2 RR	1.7324	B17	0.0025	S12	0.2885	J14	0.0025	J12
4 RR	2.4033	H5	0.0034	N11	0.2021	R14	0.0010	U16
2 RR-D	1.9025	V10	0.0050	A14	1.8715	E16	0.0043	R8

TABLE VI
ABSOLUTE RELATIVE ERROR IN QUADRANT AND CORE AVERAGE FLUX

Test case	Q-I	Q-II	Q-III	Q-IV	Core average
1 RR	0.3621	0.0194	0.0325	0.0194	0.0911
2 RR	0.3243	0.0383	0.3247	0.0378	0.1804
4 RR	0.3269	0.3076	0.3273	0.3065	0.3161
2 RR-D	0.3779	0.0794	0.3925	0.0470	0.0058

and in the case of mesh fluxes they are 0.37% and 0.51% respectively. These are of the same order as reported in [6] and [8]. From Table V it can be claimed that the maximum relative error in the estimation of channel flux from the DKF method is 2.4% which is of the same order as reported in [9].

C. Xenon-Induced Oscillations

As already stated, due to large physical dimensions, operational perturbations might lead to slow xenon-induced oscillations in AHWR. If these oscillations are left uncontrolled, the power density and time rate of change of power at some locations in the reactor core may exceed the respective design limits, resulting into increased chance of fuel failure. Therefore, to maintain the total power and power distribution within the design limits, AHWR is provided with total power control and spatial power control schemes. If due to some hypothetical reason, the spatial control scheme is ineffective, xenon-induced oscillations might occur. These xenon-induced spatial oscillations and subsequent local overpowers pose a potential threat to the fuel integrity of the reactor. Therefore, the detailed knowledge of axial and radial flux distribution in the core during the operational condition is crucial.

To ascertain this, simulation of transient involving spatial power variation was carried out using the nonlinear model of AHWR described by (36)–(40). Xenon and iodine dynamic equations [12], [14] were also incorporated in the model. The reactor was initially assumed to be under steady-state operation at full power. A small disturbance was enforced for a short duration by the simultaneous countermovement of two diagonally opposite RRs. The RR in Quadrant-I was driven 4% in, while the RR in Quadrant-III was driven 4% out simultaneously in order to maintain the net reactivity nearly zero. The response of

TABLE VII
ERROR STATISTICS IN CASE OF XENON-INDUCED SPATIAL OSCILLATIONS. (a) RMS ERROR AND RELATIVE ERROR IN FLUXES. (b) MAXIMUM AND MINIMUM RELATIVE ERROR IN CHANNELS. (c) ABSOLUTE RELATIVE ERROR IN QUADRANTS

	Quadrants (4)	Fuel locations (452)	All locations (513)	All Mesh boxes (22950)
Max. RMS Error (%)	0.1327	0.2278	0.2271	0.1746
Absolute Relative Error (%)	0.1155	0.1763	0.1741	0.1502

(a)

	Value of Error (%)	Location
Max. Negative Error	0.5385	K19
Min. Negative Error	0.0225	C15
Max. Positive Error	0.4061	U12
Min. Positive Error	0.0050	K2

(b)

Quadrant	Value of Error (%)
I	0.0554
II	0.1838
III	0.1777
IV	0.0451

(c)

model subsequent to this disturbance, was simulated for about 50 h. Reference values of mesh box fluxes were determined using (41), and SPND signals were generated using (43). Again, in these signals 2% noise was added. Now the DKF-based flux-mapping algorithm was processed for the estimation of flux distribution in AHWR. Fig. 12 shows the average values of flux in Quadrant-I, II, III, and IV of the reactor during the xenon-induced oscillations. Error analysis as described earlier has been carried out to determine the RMS percentage error and relative error (%) in flux for volume elements, channels, and quadrants. The various types of errors in estimation are given in Table VII. In general, the errors are observed to be insignificant.

From the simulations, it can be concluded that the proposed DKF algorithm can accurately estimate the time-dependent neutron flux distribution during the typical reactor operating conditions. The degradation of DKF algorithm accuracy is also very less against the detector random errors. Therefore, the proposed method can serve an effective alternate to the existing flux-mapping techniques.

VI. CONCLUSION

The neutron flux distribution in a nuclear reactor undergoes continuous variation due to routine perturbations, nonuniform burn-up at different locations, etc. The operating procedure and core control philosophy generally ensure that the time-dependent flux variations are maintained within prescribed limits. However, the flux profile is continuously monitored and displayed to the operator. The knowledge of flux distribution in the reactor core during its operation is helpful to the operator in planning of refueling scheme as well as in zonal power correction. We have suggested a novel technique based on the two-time-scale formulation of the Kalman filtering problem for the time-dependent neutron diffusion equation to near-optimum estimation of the core flux profile in AHWR. The important aspect of our technique is that it attempts solving for smaller order state prediction equations, process covariance matrices and Kalman gain. This is accomplished easily while direct solution of the Kalman filter equations is not feasible for the AHWR. Moreover, it yields excellent accuracy in flux estimation as evident from simulation exercises.

Before deployment in the AHWR, the efficacy of the technique needs to be established further, and it should be demonstrated using plant data, such as from PHWRs that it yields improvement in accuracy compared to that resulting from existing techniques. It should also be assessed from the viewpoint of implementation that the computations could be performed in real-time using hardware and other resources, suitable for control and instrumentation systems in nuclear reactors.

ACKNOWLEDGMENT

The authors would like to thank Shri A. K. Mishra, Shri M. Naskar, and Dr. S. R. Shimjith of the Reactor Control Systems Design Section, Electronics and Instrumentation (E&I) Group, Bhabha Atomic Research Centre for providing required data. The authors also wish to express their sincere thanks to Shri Y. S. Mayya (Director, E&I Group) of the Bhabha Atomic Research Centre for his encouragement and support.

REFERENCES

[1] E. Hinchley and G. Kugler, “On-line control of the CANDU PHW power distribution,” in *IAEA Specialists Meet. on Spatial Control Problems*, Studsvik, Sweden, Oct. 1974.
[2] L. Fu, L. Zhengpei, and H. Yongming, “Harmonics synthesis method for core flux distribution reconstruction,” *Prog. Nucl. Energy*, vol. 31, no. 4, pp. 369–372, 1997.
[3] M. E. Pomerantz, C. R. Calabrese, and C. Grant, “Nuclear reactor power and flux distribution fitting from a diffusion theory model and experimental data,” *Ann. Nucl. Energy*, vol. 29, no. 9, pp. 1073–1083, 2002.
[4] C. Wang, H. Wu, L. Cao, and P. Yang, “On-line reconstruction of in-core power distribution by harmonics expansion method,” *Nucl. Eng. Design*, vol. 241, no. 8, pp. 3042–3050, 2011.
[5] H. Kokame and Y. Hattori, “Kalman filter applied to estimation of neutron flux distribution and optimum allocation of in-core detectors,” *J. Nucl. Sci. Tech.*, vol. 14, no. 10, pp. 695–704, 1977.
[6] C. J. Jeong and N. Z. Cho, “Power mapping in a canada deuterium uranium reactor using kalman filtering technique,” *J. Nucl. Sci. Tech.*, vol. 37, no. 9, pp. 758–768, 2000.
[7] H. Ezure, “Estimation of most probable power distribution in BWRs by least squares method using in-core measurements,” *J. Nucl. Sci. Tech.*, vol. 25, no. 9, pp. 731–740, 1988.

[8] K. Lee and C. H. Kim, "The least-squares method for three-dimensional core power distribution monitoring in pressurized water reactors," *Nucl. Sci. Eng.*, vol. 143, no. 3, pp. 268–280, 2003.
[9] I. S. Hong, C. H. Kim, and H. C. Suk, "Advanced online flux mapping of CANDU PHWR by least-squares method," *Nucl. Sci. Eng.*, vol. 150, no. 3, pp. 299–309, 2005.
[10] S. Mishra, R. S. Modak, and S. Ganesan, "Computational schemes for online flux mapping system in a large-sized pressurized heavy water reactor," *Nucl. Sci. Eng.*, vol. 170, no. 3, pp. 280–289, 2012.
[11] R. K. Sinha and A. Kakodkar, "Design and development of the AHWR the Indian thorium fuelled innovative nuclear reactor," *Nucl. Eng. Design*, vol. 236, no. 7, pp. 683–700, 2006.
[12] S. R. Shimjith, A. P. Tiwari, M. Naskar, and B. Bandyopadhyay, "Space-time kinetics modeling of advanced heavy water reactor for control studies," *Ann. Nucl. Energy*, vol. 37, no. 3, pp. 310–324, 2010.
[13] Y. V. Sagar, A. P. Tiwari, S. R. Shimjith, M. Naskar, and S. Degweker, "Space-time kinetics modeling for the determination of neutron detector signals in advanced heavy water reactor," in *Proc. IEEE Int. Conf. Contr. Applications (CCA)*, 2013, pp. 1224–1229.
[14] S. R. Shimjith, A. P. Tiwari, B. Bandyopadhyay, and R. K. Patil, "Spatial stabilization of advanced heavy hater reactor," *Ann. Nucl. Energy*, vol. 38, no. 7, pp. 1545–1558, 2011.
[15] S. R. Shimjith, A. P. Tiwari, and B. Bandyopadhyay, "Design of fast output sampling controller for three-time-scale systems: Application to spatial control of advanced heavy water reactor," *IEEE Trans. Nucl. Sci.*, vol. 58, no. 6, pp. 3305–3316, Dec. 2011.
[16] S. R. Shimjith, A. P. Tiwari, and B. Bandyopadhyay, "A three-time-scale approach for design of linear state regulator for spatial control of advanced heavy water reactor," *IEEE Trans. Nucl. Sci.*, vol. 58, no. 3, pp. 1264–1276, Jun. 2011.
[17] R. K. Munje, B. M. Patre, S. R. Shimjith, and A. P. Tiwari, "Sliding mode control for spatial stabilization of advanced heavy water reactor," *IEEE Trans. Nucl. Sci.*, vol. 60, no. 4, pp. 3040–3050, Aug. 2013.
[18] P. V. Kokotovic, "A Riccati equation for block-diagonalization of ill-conditioned systems," *IEEE Trans. Autom. Contr.*, vol. AC-20, no. 6, pp. 812–814, Dec. 1975.
[19] P. V. Kokotovic, R. E. O'malley, and P. Sannuti, "Singular perturbations and order reduction in control theory an overview," *Automatica*, vol. 12, no. 2, pp. 123–132, 1976.
[20] J. H. Chow and P. V. Kokotovic, "A decomposition of near-optimum regulators for systems with slow and fast modes," *IEEE Trans. Autom. Contr.*, vol. AC-21, no. 5, pp. 701–705, Oct. 1976.
[21] P. V. Kokotovic, J. J. Allemong, J. R. Winkelman, and J. H. Chow, "Singular perturbation and iterative separation of time scales," *Automatica*, vol. 16, no. 1, pp. 23–33, 1980.
[22] P. V. Kokotovic, "Applications of singular perturbation techniques to control problems," *SIAM Rev.*, vol. 26, no. 4, pp. 501–550, 1984.
[23] A. K. Rao and D. S. Naidu, "Singular perturbation method for Kalman filter in discrete systems," *IEE Proc. D (Control Theory Appl.)*, vol. 131, no. 1, pp. 39–46, 1984.
[24] X. Shen, M. Rao, and Y. Ying, "Decomposition method for solving Kalman filter gains in singularly perturbed systems," *Optimal Contr. Appl. Methods*, vol. 14, no. 1, pp. 67–73, 1993.
[25] H. M. Oloomi and C. Pomalaza-Raez, "Two time scale discrete kalman filter design for an F-8 aircraft," in *Proc. Tactical Commun. Conf.*, 1996, pp. 517–522, IEEE.
[26] H. Kando, "State estimation of stochastic singularly perturbed discrete-time systems," *Opt. Cont. Appl. Methods*, vol. 18, no. 1, pp. 15–28, 1997.
[27] S. Kyu-Hong and M. E. Sawan, "Kalman filter design for singularly perturbed systems by unified approach using delta operators," in *Proc. IEEE Amer. Contr. Conf.*, 1999, vol. 6, pp. 3873–3877.
[28] V. R. Saksena, J. O'Reilly, and P. V. Kokotovic, "Singular perturbations and time-scale methods in control theory: Survey 1976-1983," *Automatica*, vol. 20, no. 3, pp. 273–293, 1984.
[29] A. Gelb, *Applied Optimal Estimation*. Cambridge, MA, USA: MIT Press, 1974.
[30] P. S. Maybeck, "Stochastic models, estimation, and control," *Math. Sci. Eng.*, vol. 141, 1979.
[31] A. Rajasekhar, A. P. Tiwari, and M. N. Belur, "Application of model order reduction techniques to space-time kinetics model of AHWR," in *Proc. IEEE Int. Conf. Industrial Instrum. and Contr. (ICIC)*, 2015, pp. 873–878.
[32] A. K. Mishra, S. R. Shimjith, T. U. Bhatt, and A. P. Tiwari, "Kalman filter-based dynamic compensator for vanadium self powered neutron detectors," *IEEE Trans. Nucl. Sci.*, vol. 61, no. 3, pp. 1360–1368, Jun. 2014.